Chapter 4

Subgrid-Based Wall Function: UMIST-*N*

4.1 Assumptions & Methodology

Before going into the details of the new wall function, it is useful to highlight the similarities between standard wall functions and the new wall function. Firstly, the new wall function uses the same grid as would be used with standard wall functions, where there is a large near-wall cell that spans entirely the viscous sublayer[1]. Secondly, like standard wall functions, the new wall function returns values of the wall shear stress and average source terms, such as $\overline{P_k}$ and $\overline{\varepsilon}$, and these terms are employed in the discretized equations in exactly the same way as with standard wall functions (see Chapter 3). Thirdly, the new wall function can be used with any level of turbulence closure and it can be easily modified to be used in any flow geometry or coordinate system (axisymmetric, 3-*D*, non-orthogonal etc.).

The primary difference between the new wall function and standard treatments is that the new wall function does not use any assumed profiles of velocity or length scale. Instead, profiles of the mean flow and turbulence parameters near the wall are obtained by solving simplified boundary-layer-type transport equations using a fine "subgrid" spanning the wall-adjacent control volume (see Figure 4.1). The wall function differs from standard low-*Re* treatments in that it decouples the numerical solution of the near-wall region from that of the main region of the flow domain and also because it does not involve the solution of the pressure-correction equation over the subgrid. The new wall function therefore does not suffer from the slow convergence problems of a full low-*Re* calculation.

The transport equations solved by the wall function across the subgrid account for convection (both parallel and normal to the wall), pressure gradient, diffusion normal to the wall and source terms. In the present study, a linear and a non-linear $k-\varepsilon$ model have been tested and so simplified *k*- and $\tilde{\varepsilon}$-equations have been solved in the wall function in addition to equations for the wall-parallel velocity components and temperature (where a thermal field is solved). The subgrid transport equations are

[1]Typically the y^+ of the near-wall node should be in the range $30 \rightarrow 300$. However, the new wall function is not reliant upon the velocity log-law and low-Reynolds-number model equations are solved throughout the domain so the cell size can be varied above and below these limits.

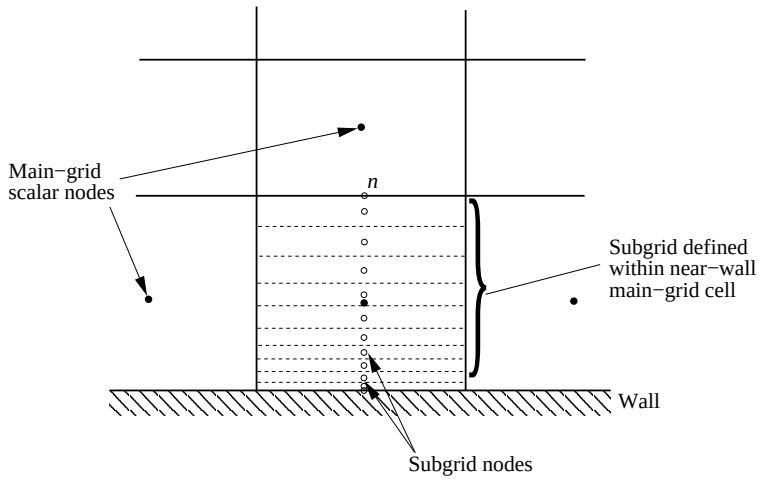

Figure 4.1: Subgrid arrangement within near-wall main-grid control volume

discretized in a similar manner to that used for simple one-dimensional diffusion problems and solved using a Tri-Diagonal Matrix Algorithm (TDMA). The wall-normal V-velocity in the near-wall cell is calculated from continuity within each of the subgrid cells and is scaled to ensure that the subgrid V-velocity at the outer edge of the subgrid (position n in Figure 4.1) is consistent with the main-grid wall-normal velocity at that location. One subgrid iteration is performed for each main-grid iteration so the subgrid solution converges as the main-grid solution converges. After each subgrid iteration, average values of the source terms across the subgrid are calculated (e.g. $\overline{P_k}$, $\overline{\varepsilon}$), along with the wall shear stress and, if the thermal field is being solved, the wall heat flux or wall temperature. These quantities are then applied as modified source terms in the main-grid near-wall cells as would be done in a standard wall-function approach. However, both the k- and ε-equations are solved in the main-grid near-wall cell, unlike the standard wall functions documented earlier which only solved for k and prescribed ε. In addition, low-Reynolds-number damping terms are included in the main-grid transport equations to enable unlimited refinement of the grid near the wall.

As was mentioned in the Introduction, the new wall function has been developed at UMIST as part of a concerted effort to find accurate and efficient alternatives to standard log-law-based wall functions. The new wall function is called UMIST-*N*: Unified Modelling through Integrated Sublayer Treatment - a *N*umerical approach.

4.2 Governing Equations

A number of assumptions are applied within the subgrid in order to obtain a simplified set of transport equations: only the momentum equation(s) parallel to the wall are solved, the diffusion parallel to the wall is assumed to be negligible in comparison to that normal to the wall, and the pressure gradient is assumed to be constant across the near-wall main-grid cell. These assumptions are applied to the Reynolds-averaged Navier-Stokes equations for momentum, energy and appropriate turbulence pa-

rameters. The current version of the wall function uses the low-Reynolds-number Launder & Sharma $k-\varepsilon$ model [13] and the non-linear EVM of Craft *et al*. [30] but in principle any turbulence model that can be integrated all the way to the wall can be used (e.g. one-equation model, $k-\omega$, DSM).

The Navier-Stokes equations are often presented in Cartesian tensor form to express succinctly the physical meaning of the various components (convection, diffusion, pressure gradient etc.) without the complicated and perhaps unfamiliar terms introduced by more general coordinate systems. However, for flows involving curved or complex-shaped walls one is forced to use body-fitted grids and the transport equations must be expressed in curvilinear coordinates. The subgrid wall function was initially developed with reference to flows in fairly simple geometries using a Cartesian grid: the channel flow, impinging jet and spinning disc flows. The governing equations which were used in these test cases are presented below (for simple 2-*D* flow) and in Appendix A for 2-*D*/axisymmetric flows involving swirl. Subgrid transport equations for the more general non-orthogonal curvilinear coordinate system are also summarized below, with a full derivation of these expressions being given in Appendix D.

4.2.1 2-*D* Cartesian Grid

In a simple 2-*D* Cartesian geometry, transport equations are solved across the subgrid for the wall-parallel U-momentum, turbulent kinetic energy, k, isotropic dissipation rate, $\tilde{\varepsilon}$, and for cases in which the thermal field is solved, temperature, T. These four subgrid transport equations are written as follows for steady incompressible flow:

$$\rho U\frac{\partial U}{\partial x}+\rho V\frac{\partial U}{\partial y}=-\frac{\mathrm{d}P}{\mathrm{d}x}+\frac{\partial}{\partial y}\left[\mu\frac{\partial U}{\partial y}-\rho\overline{uv}\right] \tag{4.1}$$

$$\rho U\frac{\partial k}{\partial x}+\rho V\frac{\partial k}{\partial y}=\frac{\partial}{\partial y}\left[\left(\mu+\frac{\mu_t}{\sigma_k}\right)\frac{\partial k}{\partial y}\right]+P_k-\rho\varepsilon \tag{4.2}$$

$$\rho U\frac{\partial \tilde{\varepsilon}}{\partial x}+\rho V\frac{\partial \tilde{\varepsilon}}{\partial y}=\frac{\partial}{\partial y}\left[\left(\mu+\frac{\mu_t}{\sigma_\varepsilon}\right)\frac{\partial \tilde{\varepsilon}}{\partial y}\right]+c_{\varepsilon 1}f_1P_k\frac{\tilde{\varepsilon}}{k}-c_{\varepsilon 2}f_2\rho\frac{\tilde{\varepsilon}^2}{k}+\rho Y_c+P_{\varepsilon 3} \tag{4.3}$$

$$\rho U\frac{\partial T}{\partial x}+\rho V\frac{\partial T}{\partial y}=\frac{\partial}{\partial y}\left[\left(\frac{\mu}{\sigma}+\frac{\mu_t}{\sigma_t}\right)\frac{\partial T}{\partial y}\right] \tag{4.4}$$

Each of the low-Reynolds-number damping terms appearing in the above equations has previously been discussed in Chapter 2. The pressure gradient is intentionally not expressed using partial derivatives since $\mathrm{d}P/\mathrm{d}x$ is assumed constant across the subgrid. Some of the source terms appearing in the above expressions can be simplified using the boundary-layer assumptions. For instance, the total dissipation rate (ε) which appears in the k-equation is given by:

$$\varepsilon=\tilde{\varepsilon}+2\nu\left(\frac{\partial k^{1/2}}{\partial x_j}\right)^2 \tag{4.5}$$

which is approximated in the subgrid by:

$$\varepsilon \approx \tilde{\varepsilon} + 2\nu \left(\frac{\partial k^{1/2}}{\partial y} \right)^2 \tag{4.6}$$

The differential Yap correction (see Equation 2.17) can cause some instability when it is employed in the subgrid wall function. This problem only occurs at the start of a calculation when there are rapid changes in the values of k and $\tilde{\varepsilon}$ between successive iterations. Since the subgrid k- and $\tilde{\varepsilon}$-equations are under-relaxed, they do not respond immediately to changes in the boundary conditions and, if the main-grid k and $\tilde{\varepsilon}$ fields are changing rapidly, this can lead to large length-scale gradients in the subgrid. To overcome this problem, the Yap correction in the outermost subgrid cell (farthest from the wall) is set to zero initially and is re-introduced only once the solution is nearly converged.

Linear $k-\varepsilon$ Model

Using the linear $k-\varepsilon$ EVM, the Reynolds stress is assumed to be a linear function of the mean strain rate:

$$-\overline{u_i u_j} + \frac{2}{3} k \delta_{ij} = \nu_t S_{ij} \tag{4.7}$$

where the strain-rate tensor, S_{ij}, is given by:

$$S_{ij} = \frac{\partial U_i}{\partial x_j} + \frac{\partial U_j}{\partial x_i} \tag{4.8}$$

and the kinematic eddy-viscosity, ν_t:

$$\nu_t = c_\mu f_\mu \frac{k^2}{\tilde{\varepsilon}} \tag{4.9}$$

Substituting these two expressions into the subgrid wall-parallel momentum equation one obtains:

$$\rho U \frac{\partial U}{\partial x} + \rho V \frac{\partial U}{\partial y} = -\frac{\mathrm{d}P}{\mathrm{d}x} - \frac{\mathrm{d}}{\mathrm{d}x}\left(\frac{2}{3}\rho k\right) + \frac{\partial}{\partial y}\left[(\mu + \mu_t)\frac{\partial U}{\partial y}\right] \tag{4.10}$$

Note that the wall-parallel gradient of the isotropic stress component $2/3\rho k$ has been retained, despite the assumption stated earlier that diffusion parallel to the wall is ignored within the subgrid. This term is included for convenience since it is common practice in CFD codes to include the $2/3\rho k$ term with the pressure, so that the "pressure" which is stored in computer memory is in fact $\left(P' = P + 2\rho k/3\right)$. In tests with the impinging jet flow, discussed later, including the $2/3\rho k$ term with the subgrid pressure gradient had negligible effect.

The production of turbulent kinetic energy, P_k, used in the subgrid k and $\tilde{\varepsilon}$ equations, includes

components from all of the stresses:

$$\begin{aligned} P_k &= -\rho\overline{u_i u_j}\frac{\partial U_i}{\partial x_j} \\ &= -\rho\overline{u^2}\frac{\partial U}{\partial x} - \rho\overline{uv}\left(\frac{\partial U}{\partial y}+\frac{\partial V}{\partial x}\right) - \rho\overline{v^2}\frac{\partial V}{\partial y} \end{aligned} \tag{4.11}$$

whilst the gradient production term, $P_{\varepsilon 3}$, is simplified:

$$P_{\varepsilon 3} = 2\mu\nu_t\left(\frac{\partial^2 U_i}{\partial x_j \partial x_k}\right)^2 \approx 2\mu\nu_t\left(\frac{\partial^2 U}{\partial y^2}\right)^2 \tag{4.12}$$

The remaining damping functions in the linear $k-\varepsilon$ model of Launder & Sharma are the same as those presented in Chapter 2.

Non-Linear $k-\varepsilon$ Model

The calculation of the Reynolds stress across the subgrid using the Craft *et al*. two-equation NLEVM involves the same expressions as discussed in Section 2.3 for the main-grid. The recommendations of Craft, Iacovides & Yoon [67] are followed to maximize the numerical stability of the model, which lead to the following expression for the subgrid U-momentum:

$$\rho U\frac{\partial U}{\partial x} + \rho V\frac{\partial U}{\partial y} = -\frac{\mathrm{d}P^{'}}{\mathrm{d}x} + \frac{\partial}{\partial y}\left[\left(\mu+\mu_t'\right)\frac{\partial U}{\partial y} - \rho\widehat{\overline{uv}}\right] \tag{4.13}$$

The modified eddy-viscosity, μ_t', includes any positive contribution from the last two cubic terms in Equation (2.27), and $\widehat{\overline{uv}}$ is the remaining higher-order components of the Reynolds stress, i.e.:

$$\mu_t' = \mu_t - \mu_t\frac{k^2}{\tilde{\varepsilon}^2}\min\left[\left(c_6 S_{kl}S_{kl} + c_7\Omega_{kl}\Omega_{kl}\right),0\right] \tag{4.14}$$

$$\begin{aligned} -\widehat{\overline{uv}} &= \nu_t\frac{k}{\tilde{\varepsilon}}\left[c_1 S_{12}\left(S_{11}+S_{22}\right)\right. \\ &\quad \left. + c_2\Omega_{12}\left(S_{22}-S_{11}\right)\right] \\ &\quad + \nu_t\left(\frac{k}{\tilde{\varepsilon}}\right)^2\left[c_4\Omega_{12}\left(S_{11}^2 - S_{22}^2\right)\right. \\ &\quad \left. + S_{12}\max\left[\left(c_6 S_{kl}S_{kl} + c_7\Omega_{kl}\Omega_{kl}\right),0\right]\right] \end{aligned} \tag{4.15}$$

The only other difference between the subgrid equations and the main-grid equations presented in Section 2.3, is the simplification of the gradient production term, $P_{\varepsilon 3}$, which is approximated as:

$$\begin{aligned} P_{\varepsilon 3} &\approx 0.0022\frac{\tilde{S}\mu_t k^2}{\tilde{\varepsilon}}\left(\frac{\partial^2 U}{\partial y^2}\right)^2 \quad \text{for} \quad \tilde{R}_t \le 250 \\ &= 0 \qquad\qquad\qquad\qquad\quad \text{for} \quad \tilde{R}_t > 250 \end{aligned} \tag{4.16}$$

4.2.2 Non-Orthogonal Curvilinear Grid

There are several types of curvilinear coordinate systems. These can be divided into orthogonal and non-orthogonal curvilinear coordinate systems, which can be further subdivided into systems where the velocity vectors are either aligned with the coordinate system or are aligned to another (usually Cartesian) reference frame. For example, the STREAM code [72, 73] uses a non-orthogonal grid in which velocity vectors are aligned to a Cartesian reference frame. There are advantages to the approach used by STREAM, as discussed in [73], where it is shown that the resulting momentum equations can be expressed in "strong conservation form". However, this approach can also suffer from increased numerical diffusion when there are large skew angles between the velocity components and the faces of the computational cells [83]. In the subgrid wall function, simplified equations are solved for velocity components parallel to the wall within the subgrid region. This requires the use of a coordinate system in which velocity vectors are aligned with the wall (i.e. aligned with the curvilinear coordinate system, assuming a body-fitted grid is adopted).

The Navier-Stokes equations were derived in orthogonal curvilinear coordinates, with velocity vectors aligned to the coordinate system, by Pope [84]. Orthogonal curvilinear coordinates are attractive in that some of the mathematics can be simplified, but this approach relies upon a grid generation algorithm which ensures that grid lines intersect at right-angles throughout the domain, which is difficult to achieve in complex three-dimensional geometries. The alternative formulation of the Navier-Stokes equations in a non-orthogonal curvilinear coordinate system with velocity vectors aligned to the grid has been employed by, among others, Richmond *et al*. [83], Demirdžić *et al*. [85, 86], Gal-Chen & Somerville [87], Mynett *et al*. [88] and Lee & Soni [89].

The transport equations in non-orthogonal curvilinear coordinates are long and fairly complicated. Since it is easy to make typographical errors with such expressions, and due to the relatively unfamiliar nature of the notation to many readers, a comprehensive introduction and background has been provided in Appendix B. This should enable any errors to be traced and allow the reader to follow the derivation without recourse to additional texts. Further analysis can be found in Lien's thesis [73], which describes the fundamentals of the STREAM code. The conventions adopted in this thesis follow those of Farrashkhalvat & Miles [90] whilst, in some cases, conventions used by Demirdžić *et al*. have been used to allow direct comparison with equations given in their paper. For a general introduction to tensors see, for example, Aris [91], Simmonds [92] or McConnell [93].

The three-dimensional non-orthogonal subgrid coordinate system has directional components (ξ,η,ζ). Throughout this thesis, it is assumed that the ξ- and η-components are aligned to grid lines which are parallel to the wall whilst the ζ-axis is usually, but not necessarily, wall-normal (i.e. not wall-parallel), see Figure 4.2. The subgrid transport equations can all be written in the following generic form:

$$\frac{\rho U}{\sqrt{g_{11}}}\left(\frac{\partial\phi}{\partial\xi}\right)^{*}+\frac{\rho V}{\sqrt{g_{22}}}\left(\frac{\partial\phi}{\partial\eta}\right)^{*}+\frac{\rho W}{\sqrt{g_{33}}}\left(\frac{\partial\phi}{\partial\zeta}\right)^{*}=\frac{1}{J}\frac{\partial}{\partial\zeta}\left(Jg^{33}\Gamma\frac{\partial\phi}{\partial\zeta}\right)+C \tag{4.17}$$

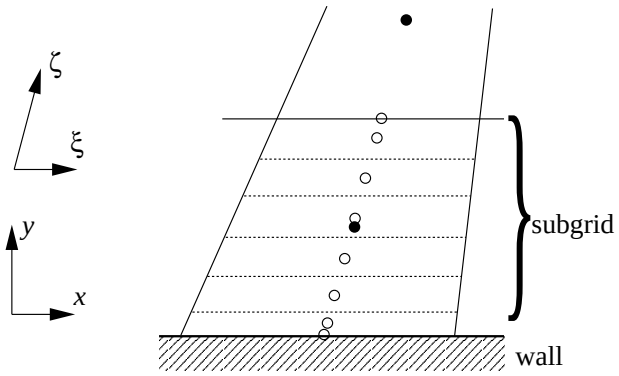

Figure 4.2: Typical non-orthogonal arrangement of subgrid cells showing Cartesian $x-y$ axis and curvilinear $\xi-\zeta$ axes.

where ϕ denotes one of the subgrid parameters: U, V, k or $\tilde{\varepsilon}$, Γ is the diffusivity and the source term, C, includes geometry-related source terms, the pressure gradient in the momentum equations and production and dissipation sources in the k- and $\tilde{\varepsilon}$-equations. The velocity components U, V and W act in the ξ, η and ζ directions respectively and are "physical" velocities, i.e. they have units of (length/time). Gradient terms appearing in the convection are discretized using upwind differencing. The asterisk $(^*)$ denotes the fact that, for some quantities, the upstream values of ϕ appearing in the discretized convection terms are transformed from the coordinate system used in the upstream cell into the current cell coordinate system. This transformation only affects the convection of momentum where the direction of the velocity vectors in the upstream cell may differ from those in the current cell. Since scalar parameters (k and $\tilde{\varepsilon}$) are invariant to the reference frame, the upstream values of scalars do not have to undergo such transformations. The $\sqrt{g_{11}}$, $\sqrt{g_{22}}$ and $\sqrt{g_{33}}$ terms (square-roots of the covariant metric tensor components) are equivalent to the physical widths of the cells in the ξ, η and ζ directions respectively. When the above transport equation is discretized, as discussed later, it is assumed that the widths of the computational cells in the three coordinate directions are unity, i.e. $\Delta\xi = \Delta\eta = \Delta\zeta = 1$. It can be seen, then, that the convection terms in the above expression are equivalent to their counterparts in Cartesian coordinates, i.e.:

$$\frac{\rho U}{\sqrt{g_{11}}}\frac{\partial\phi}{\partial\xi} \rightarrow \rho U\frac{\partial\phi}{\partial x} \tag{4.18}$$

The diffusion term in the above generic transport equation involves two geometric symbols: the Jacobian, J, and the contravariant metric tensor, g^{33}. For cells of unit dimensions ($\Delta\xi = \Delta\eta = \Delta\zeta = 1$), the Jacobian is simply the physical cell volume whilst the g^{33} tensor is equivalent to the square of the area of the face in the wall-parallel $\xi-\eta$ plane (A_{12}) divided by the cell volume squared, i.e.:

$$g^{33} = \left(\frac{A_{12}}{J}\right)^2 \tag{4.19}$$

In a Cartesian system this is simply the inverse of the cell height squared, $g^{33} = (1/\Delta z)^2$, if the wall is in the $x-y$ plane. Substituting this into the diffusion term, we obtain:

$$\frac{1}{J}\frac{\partial}{\partial\zeta}\left[\frac{(A_{12})^2}{J}\Gamma\frac{\partial\phi}{\partial\zeta}\right] \tag{4.20}$$

If this is discretized and integrated over the physical cell volume ($\Delta Vol = J\Delta\xi\Delta\eta\Delta\zeta$), the coefficients associated with the top and bottom nodes in the discretized equation (a_T and a_B) are of the form:

$$\frac{\Gamma A}{L} \tag{4.21}$$

where A is the cell-face area and L is the vertical distance between adjacent nodes. This is identical to the expression obtained when a Cartesian coordinate system is employed. In the linear and non-linear $k-\varepsilon$ models used in the present study, the diffusivity for the wall-parallel momentum equations is:

$$\Gamma = \mu + \mu_t = \mu_{eff} \tag{4.22}$$

and for the k and ε equations:

$$\Gamma_k = \mu + \frac{\mu_t}{\sigma_k} \tag{4.23}$$

$$\Gamma_\varepsilon = \mu + \frac{\mu_t}{\sigma_\varepsilon} \tag{4.24}$$

Wall-Parallel Momentum

The transport equation for the wall-parallel momentum is lengthy and complicated since, on a curved grid, the coordinate axes to which the velocity vectors are aligned change between neighbouring cells. The momentum equation thus has to take into account the fact that the U-velocity in one cell may be pointing in a different direction to the U-velocity in an adjacent cell. The subgrid wall-parallel U- and V-momentum equations are written:

$$\frac{\rho U}{\sqrt{g_{11}}}\left(\frac{\partial U}{\partial\xi}\right)^* + \frac{\rho V}{\sqrt{g_{22}}}\left(\frac{\partial U}{\partial\eta}\right)^* + \frac{\rho W}{\sqrt{g_{33}}}\left(\frac{\partial U}{\partial\zeta}\right)^* = \frac{1}{J}\frac{\partial}{\partial\zeta}\left(Jg^{33}\Gamma\frac{\partial U}{\partial\zeta}\right) + C^1 \tag{4.25}$$

$$\frac{\rho U}{\sqrt{g_{11}}}\left(\frac{\partial V}{\partial\xi}\right)^* + \frac{\rho V}{\sqrt{g_{22}}}\left(\frac{\partial V}{\partial\eta}\right)^* + \frac{\rho W}{\sqrt{g_{33}}}\left(\frac{\partial V}{\partial\zeta}\right)^* = \frac{1}{J}\frac{\partial}{\partial\zeta}\left(Jg^{33}\Gamma\frac{\partial V}{\partial\zeta}\right) + C^2 \tag{4.26}$$

The source term, C^i, can be summarized as follows:

$$\begin{aligned} C^i \quad = \quad & \underbrace{-\tau^{ij}\frac{\Gamma^m_{ij}g_{im}}{\sqrt{g_{ii}}}+\tau^{mj}\Gamma^i_{mj}\sqrt{g_{ii}}}_{diffusion\ I} \\ & \underbrace{+\frac{1}{J}\frac{\partial}{\partial\zeta}\left[J\mu_{eff}g^{33}\left(U^{(m)}\frac{\sqrt{g_{ii}}}{\sqrt{g_{mm}}}\Gamma^i_{m3}-U\frac{g_{im}}{g_{ii}}\Gamma^m_{i3}\right)\right]}_{diffusion\ II} \\ & \underbrace{-g^{ij}\sqrt{g_{ii}}\frac{\partial P'}{\partial\xi^j}}_{pressure\ gradient} \\ & \text{no summation on } i \end{aligned} \tag{4.27}$$

where $i = 1$ and 2 for the U- and V-momentum equations respectively. The velocities, (U,V,W) in the three component directions (ξ,η,ζ) are denoted $U^{(j)}$, where the parenthesis is used to emphasize the fact that the velocities are "physical". The Γ^m_{ij} terms are Christoffel symbols of the second kind which result from having a non-uniform grid distribution. These terms will be non-zero if, for example, the grid cells are clustered together towards the wall or if the wall is curved.

Calculation of the Stress, τ^{ij}

The non-physical stress tensor, τ^{ij}, for incompressible flow is given by:

$$\tau^{ij} = \mu\left(g^{jm}U^i_{,m}+g^{im}U^j_{,m}\right)-\rho\overline{u^iu^j} \tag{4.28}$$

For a linear $k-\varepsilon$ model, the Reynolds stress, $\overline{u^iu^j}$, is given by:

$$\overline{u^iu^j} = -\nu_t S^{ij}+\frac{2}{3}g^{ij}k \tag{4.29}$$

where the strain-rate, S^{ij}, is:

$$S^{ij} = \left(g^{jm}U^i_{,m}+g^{im}U^j_{,m}\right) \tag{4.30}$$

and the velocity gradient, $U^i_{,j}$:

$$U^i_{,j} \quad = \quad \frac{\partial}{\partial\xi^j}\left(\frac{U^{(i)}}{\sqrt{g_{ii}}}\right)+\frac{U^{(m)}}{\sqrt{g_{mm}}}\Gamma^i_{mj} \tag{4.31}$$

For the non-linear $k-\varepsilon$ model of Craft *et al*. the Reynolds stress, $\overline{u^i u^j}$, is given by:

$$\begin{aligned}
\overline{u^i u^j} &= -\nu_t S^{ij} + \frac{2}{3} g^{ij} k \\
&+ c_1 \frac{\nu_t k}{\tilde{\varepsilon}} \left(g_{kl} S^{ik} S^{jl} - \frac{1}{3} g_{km} g_{ln} S^{kl} S^{mn} g^{ij} \right) \\
&+ c_2 \frac{\nu_t k}{\tilde{\varepsilon}} \left(g_{kl} \Omega^{ik} S^{jl} + g_{kl} \Omega^{jk} S^{il} \right) \\
&+ c_3 \frac{\nu_t k}{\tilde{\varepsilon}} \left(g_{kl} \Omega^{ik} \Omega^{jl} - \frac{1}{3} g_{km} g_{ln} \Omega^{kl} \Omega^{mn} g^{ij} \right) \\
&+ c_4 \frac{\nu_t k^2}{\tilde{\varepsilon}^2} \left(S^{ki} \Omega^{lj} + S^{kj} \Omega^{li} \right) g_{lm} g_{kn} S^{mn} \\
&+ c_5 \frac{\nu_t k^2}{\tilde{\varepsilon}^2} \left(g_{kl} g_{mn} \Omega^{ik} \Omega^{ln} S^{mj} + g_{kl} g_{mn} S^{ik} \Omega^{ln} \Omega^{mj} - \frac{2}{3} g_{kl} g_{mo} g_{np} S^{km} \Omega^{on} \Omega^{pl} g^{ij} \right) \\
&+ c_6 \frac{\nu_t k^2}{\tilde{\varepsilon}^2} g_{km} g_{ln} S^{ij} S^{ml} S^{kn} \\
&+ c_7 \frac{\nu_t k^2}{\tilde{\varepsilon}^2} g_{km} g_{ln} S^{ij} \Omega^{ml} \Omega^{kn}
\end{aligned} \tag{4.32}$$

Fortunately the constant c_5 in the Craft *et al*. model is zero so there is no need to expand one line of the above expression. The recommended practice of including the c_6 and c_7 terms with the linear component is used, as for the Cartesian formulation. For details see Appendix D.

Calculation of the Pressure Gradient

Returning to the expression for the source term, C, (Equation 4.27), the final pressure gradient term involves gradients of the effective pressure in all three coordinate directions. For example the U-momentum equation pressure term is given by:

$$g^{ij} \sqrt{g_{ii}} \frac{\partial P'}{\partial \xi^j} = \sqrt{g_{11}} \left(g^{11} \frac{\partial P'}{\partial \xi} + g^{12} \frac{\partial P'}{\partial \eta} + g^{13} \frac{\partial P'}{\partial \zeta} \right) \tag{4.33}$$

where $\left(P' = P + 2\rho k/3 \right)$ is used for convenience as with the Cartesian formulation. If the subgrid cells are arranged such that the ζ-axis is orthogonal to the wall, then the contravariant metric tensor, g^{13}, is zero and there is no contribution from the $\partial P'/\partial \zeta$ term in the above expression. However, if the cells are skewed and the ζ-axis is no longer normal to the wall, g^{13} is finite and the $\partial P'/\partial \zeta$ term may become significant. Effectively, this is saying that when the cells are skewed relative to the wall, the pressure gradient in the ζ-direction has a component that is parallel to the wall. Whilst this may at first seem a relatively simple problem to solve, on closer inspection it becomes apparent that one needs to know how the pressure changes across the near-wall region (even though one does not solve for the pressure across the subgrid). To obtain a truly accurate representation of the pressure distribution across the subgrid for complex flows one would have to solve elliptic equations which would defeat

the purpose of the wall function (since effectively one would be obtaining a full low-Reynolds-number model solution). On the other hand, simply prescribing an arbitrary shape for the $\partial P^{'}/\partial\zeta$ profile is unlikely to be general enough for the wall function to work in a variety of complex flows. Instead, the following expression is solved across the subgrid:

$$\nabla P \cdot \hat{\mathbf{n}} + (\nabla \cdot \rho\overline{\mathbf{u} \otimes \mathbf{u}}) \cdot \hat{\mathbf{n}} = 0 \tag{4.34}$$

where $\hat{\mathbf{n}}$ is the unit wall-normal vector, $\overline{\mathbf{u} \otimes \mathbf{u}}$ is the Reynolds stress in vector form and the gradient operator, ∇, can be written for non-orthogonal coordinates as:

$$\nabla = \frac{\partial \xi^j}{\partial x^i}\frac{\partial}{\partial \xi^j}\mathbf{e}_i \tag{4.35}$$

where $\mathbf{e}_i$ is the Cartesian unit vector and $\partial\xi^j/\partial x^i$ is a property of the grid. This expression is identical to that used in the STREAM code to evaluate the pressure on the wall surface (see Section 3.3.5).

Turbulent Kinetic Energy, k

The subgrid k-equation in curvilinear coordinates is as follows:

$$\frac{\rho U}{\sqrt{g_{11}}}\frac{\partial k}{\partial \xi} + \frac{\rho V}{\sqrt{g_{22}}}\frac{\partial k}{\partial \eta} + \frac{\rho W}{\sqrt{g_{33}}}\frac{\partial k}{\partial \zeta} = \frac{1}{J}\frac{\partial}{\partial \zeta}\left[Jg^{33}\left(\mu + \frac{\mu_t}{\sigma_k}\right)\frac{\partial k}{\partial \zeta}\right] + P_k - \rho\varepsilon \tag{4.36}$$

The production rate source term is given by:

$$P_k = -\rho g_{im}\overline{u^j u^m}U^i_{,j} \tag{4.37}$$

and is expanded fully (including all the shear and normal stress components). The expressions for the Reynolds stresses are given above for the linear and non-linear models (Equations 4.29 and 4.32 respectively) and the velocity gradient, $U^i_{,j}$, is given by Equation (4.31). The expression for the total dissipation rate is simplified by considering only the gradient of $k^{1/2}$ parallel to the ζ-axis:

$$\begin{aligned} \varepsilon &= \tilde{\varepsilon} + 2\nu g^{jm}\left(\frac{\partial k^{1/2}}{\partial \xi^m}\right)\left(\frac{\partial k^{1/2}}{\partial \xi^j}\right) \\ &\approx \tilde{\varepsilon} + 2\nu g^{33}\left(\frac{\partial k^{1/2}}{\partial \zeta}\right)\left(\frac{\partial k^{1/2}}{\partial \zeta}\right) \end{aligned} \tag{4.38}$$

Isotropic Dissipation Rate, $\tilde{\varepsilon}$

The subgrid $\tilde{\varepsilon}$-equation in curvilinear coordinates is as follows:

$$\begin{aligned}\frac{\rho U}{\sqrt{g_{11}}}\frac{\partial\tilde{\varepsilon}}{\partial\xi}+\frac{\rho V}{\sqrt{g_{22}}}\frac{\partial\tilde{\varepsilon}}{\partial\eta}+\frac{\rho W}{\sqrt{g_{33}}}\frac{\partial\tilde{\varepsilon}}{\partial\zeta} &= \frac{1}{J}\frac{\partial}{\partial\zeta}\left[Jg^{33}\left(\mu+\frac{\mu_t}{\sigma_\varepsilon}\right)\frac{\partial\tilde{\varepsilon}}{\partial\zeta}\right] \\ &\quad +c_{\varepsilon1}f_1P_k\frac{\tilde{\varepsilon}}{k}-c_{\varepsilon2}f_2\rho\frac{\tilde{\varepsilon}^2}{k}+\rho Y_c+P_{\varepsilon3} \qquad (4.39)\end{aligned}$$

The source terms appearing in the $\tilde{\varepsilon}$-equation include production $(c_{\varepsilon1}f_1P_k\tilde{\varepsilon}/k)$, dissipation $\left(c_{\varepsilon2}f_2\tilde{\varepsilon}^2/k\right)$, the Yap correction (Y_c) and the near-wall gradient-production source term $(P_{\varepsilon3})$. The production term has already been expanded above for the *k*-equation and the dissipation term does not require further expansion. The standard Yap correction is unchanged in curvilinear coordinates and relies solely upon the wall normal distance and values of *k* and $\tilde{\varepsilon}$. The gradient of the length scale appearing in the differential Yap correction (see Equation 2.17) is simplified as follows:

$$\begin{aligned}F &= \frac{1}{c_l}\left[\left(g^{jk}\frac{\partial l}{\partial\xi^j}\frac{\partial l}{\partial\xi^k}\right)^{1/2}-dl_e dy\right] \qquad (4.40)\\ &\approx \frac{1}{c_l}\left[\left(g^{33}\frac{\partial l}{\partial\zeta}\frac{\partial l}{\partial\zeta}\right)^{1/2}-dl_e dy\right] \qquad (4.41)\end{aligned}$$

where the additional contravariant metric tensor $\left(g^{jk}\right)$ is introduced into Equation (4.40) in order to satisfy the summation convention and it is assumed that the gradient of the length scale parallel to the wall is negligible in comparison with the gradient normal to the wall. The $dl_e dy$ term is identical to that given earlier (see Equation 2.19). The same recommendations apply to the curvilinear version of the UMIST-*N* wall function as with the Cartesian formulation, namely that the differential Yap correction in the outermost subgrid cell (farthest from the wall) is set to zero initially and is re-introduced only once the solution is nearly converged.

The full expansion of the gradient production source term, $P_{\varepsilon3}$, in curvilinear coordinates is given by:

$$P_{\varepsilon3}=2\mu\nu_t g_{im}g_{jn}g^{lp}\left(g^{no}U^m_{,o}\right)_{,p}\left(g^{jk}U^i_{,k}\right)_{,l} \qquad (4.42)$$

where the double-derivative of the velocity component is given by:

$$\left(g^{jk}U^i_{,k}\right)_{,l}=\frac{\partial\left(g^{jk}U^i_{,k}\right)}{\partial\xi^l}+g^{jk}U^m_{,k}\Gamma^i_{ml}+g^{mk}U^i_{,k}\Gamma^j_{ml} \qquad (4.43)$$

To simplify this term, it is assumed that only the gradient of the wall-parallel velocity components in the wall-normal direction are significant (i.e. $k=l=o=p=3$ and $i=m=1,2$):

$$P_{\varepsilon3}=2\mu\nu_t\left[g_{11}g_{jn}g^{33}\left(g^{n3}U_{,3}\right)_{,3}\left(g^{j3}U_{,3}\right)_{,3}+g_{22}g_{jn}g^{33}\left(g^{n3}V_{,3}\right)_{,3}\left(g^{j3}V_{,3}\right)_{,3}\right] \qquad (4.44)$$

where the double-derivative term is obtained from:

$$\left(g^{j3}U^i_{,3}\right)_{,3} = \frac{\partial\left(g^{j3}U^i_{,3}\right)}{\partial\zeta} + g^{j3}\left(U_{,3}\Gamma^i_{13} + V_{,3}\Gamma^i_{23}\right) + U^i_{,3}\left(g^{13}\Gamma^j_{13} + g^{23}\Gamma^j_{23} + g^{33}\Gamma^j_{33}\right) \tag{4.45}$$

It is assumed that the derivative of the W-velocity in the wall-normal ζ-direction is negligible in comparison with the other contributions. The above expressions require the values of strain-rates $U_{,3}$ and $V_{,3}$, the contravariant metric tensor g^{33} and the Jacobian, J to be calculated at the top and bottom subgrid cell boundaries (in the ζ-direction). These are found from linear interpolation of the physical velocity components, U and V, and the Christoffel symbols, between adjacent nodal values.

4.3 Implementation

In the previous section the subgrid transport equations were presented for a simple two-dimensional Cartesian geometry and the more complex non-orthogonal curvilinear coordinate system. The discretization and implementation of these two sets of transport equations is fundamentally the same and so for clarity, the following section describes the implementation of UMIST-*N* in a 2-*D* Cartesian geometry. See Appendix E for details of the non-orthogonal case.

4.3.1 Discretized Equations

The subgrid transport equations for wall-parallel velocity, U, turbulent kinetic energy, k, isotropic dissipation rate, $\tilde{\varepsilon}$, and temperature , T, can all be expressed in the general form:

$$\rho U\frac{\partial\phi}{\partial x} + \rho V\frac{\partial\phi}{\partial y} = \frac{\partial}{\partial y}\left(\Gamma\frac{\partial\phi}{\partial y}\right) + C \tag{4.46}$$

where ϕ is either U, k, $\tilde{\varepsilon}$ or T, Γ is the relevant diffusivity and C includes all the source terms.

1-*D* Diffusion

If one firstly considers only the diffusion and source terms in the above expression:

$$\frac{\partial}{\partial y}\left(\Gamma\frac{\partial\phi}{\partial y}\right) + C = 0 \tag{4.47}$$

where C is assumed constant across each cell. Applying the finite-volume approach (see Section 3.1): integrating the transport equation across a subgrid cell and using central differencing to evaluate gradients, the above equation becomes:

$$\Gamma_n A_n\frac{(\phi_N - \phi_P)}{\Delta y_{NP}} - \Gamma_s A_s\frac{(\phi_P - \phi_S)}{\Delta y_{PS}} + (C)_P\,\Delta Vol = 0 \tag{4.48}$$

where A is the cross-sectional area of the cell, ΔVol is the cell volume, subscripts n and s refer to the north and south boundaries and P, N and S to the current, northern and southern nodes, Δy_{NP} is the distance from node N to node P, and Δy_{PS} the distance from node P to node S, as shown in Figure 4.3. Simplifying this expression one obtains:

$$D_n(\phi_N - \phi_P) - D_s(\phi_P - \phi_S) + (C)_P \Delta Vol = 0 \tag{4.49}$$

where:

$$D_n = \frac{\Gamma_n A_n}{\Delta y_{NP}} \tag{4.50}$$

$$D_s = \frac{\Gamma_s A_s}{\Delta y_{PS}} \tag{4.51}$$

Grouping coefficients of ϕ_P results in:

$$D_n\phi_N + D_s\phi_S + (C)_P \Delta Vol = (D_n + D_s)\phi_P \tag{4.52}$$

which can be expressed as:

$$a_P\phi_P = a_N\phi_N + a_S\phi_S + S \tag{4.53}$$

where:

$$a_N = D_n = \frac{\Gamma_n A_n}{\Delta y_{NP}} \tag{4.54}$$

$$a_S = D_s = \frac{\Gamma_s A_s}{\Delta y_{PS}} \tag{4.55}$$

$$a_P = a_N + a_S \tag{4.56}$$

$$S = (C)_P \Delta Vol \tag{4.57}$$

To maximize the numerical stability of the UMIST-*N* wall function calculation, the source term (S) is linearized, as discussed in Section 3.1.

Convection

There are primarily two different ways in which convection can be modelled: in conservative or non-conservative form. For a steady incompressible 2-*D* flow these can be written:

$$\text{Conservative}: \quad \frac{\partial(\rho U\phi)}{\partial x} + \frac{\partial(\rho V\phi)}{\partial y} \tag{4.58}$$

$$\text{Non}-\text{conservative}: \quad \rho U\frac{\partial\phi}{\partial x} + \rho V\frac{\partial\phi}{\partial y} \tag{4.59}$$

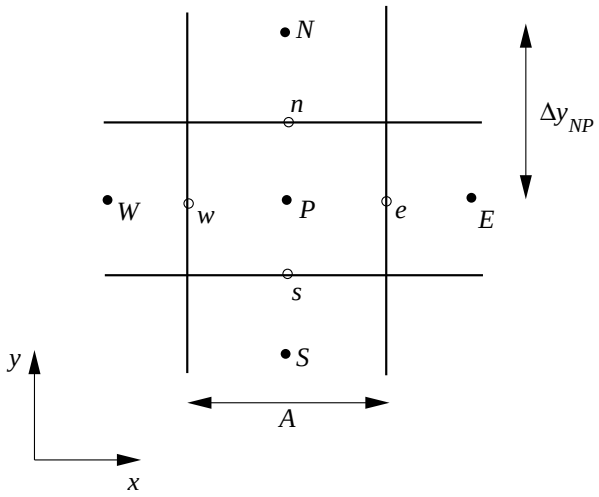

Figure 4.3: Subgrid node and boundary notation

To convert from conservative to non-conservative form one simple expands Equation (4.58) following the product rule and applies the continuity condition:

$$\frac{\partial U}{\partial x} + \frac{\partial V}{\partial y} = 0 \tag{4.60}$$

A conservative form must be used in compressible flows if a shock-capturing method is used, but it also seems to be the more common treatment for convection in incompressible flow [77].

If ϕ represents a homogeneous scalar field (such as a uniform temperature field) then, in the conservative form, any small imbalance in the mass flux though the faces of a cell can lead to finite convection, despite the field being homogeneous (i.e. ϕ is constant but since $\partial U/\partial x + \partial V/\partial y \neq 0$ then the convection is not zero). In a standard incompressible elliptic CFD code (such as the TEAM code), the coupling of velocity and pressure using the SIMPLE algorithm ensures that continuity is observed in each of the grid cells, and so the problem of spurious convection does not occur. However, the subgrid wall function is essentially a parabolic solver and only calculates the momentum parallel to the wall. The pressure gradient is treated as a constant provided by the main-grid solution and hence, within the current framework of the wall function, it is not guaranteed that mass continuity is observed within each of the subgrid cells[2]. It is, therefore, necessary to use a non-conservative convection scheme within the subgrid to avoid the problem referred to above, and to ensure that a homogeneous scalar field will result in zero convection regardless of mass continuity.

Convection parallel to the wall in non-conservative form is written:

$$\rho U \frac{\partial \phi}{\partial x} \tag{4.61}$$

The U-velocity in each of the subgrid cells is known since a transport equation for the subgrid mo-

[2]Continuity is, of course, satisfied over all the main-grid cells, including the near-wall cells.

mentum parallel to the wall is solved. The gradient in ϕ parallel to the wall is found using upwind differencing. Assuming that the velocity is positive, i.e. flowing from west to east:

$$\rho U \frac{\partial \phi}{\partial x} = \rho U_P \frac{(\phi_P - \phi_W)}{\Delta x_{PW}} \tag{4.62}$$

where the subgrid velocity, U_P, is positive and P and W refer to subgrid nodal positions[3] given in Figure 4.4. In order to calculate gradients parallel to the wall it is therefore necessary to store each of the subgrid profiles along the wall. This unfortunately leads to storage requirements of the subgrid wall function approaching those of full low-*Re* model[4]. An alternative scheme was tested during the development of UMIST-*N* which employed scaled main-grid values to calculate $\partial\phi/\partial x$ but this was found to be unstable (see Appendix G).

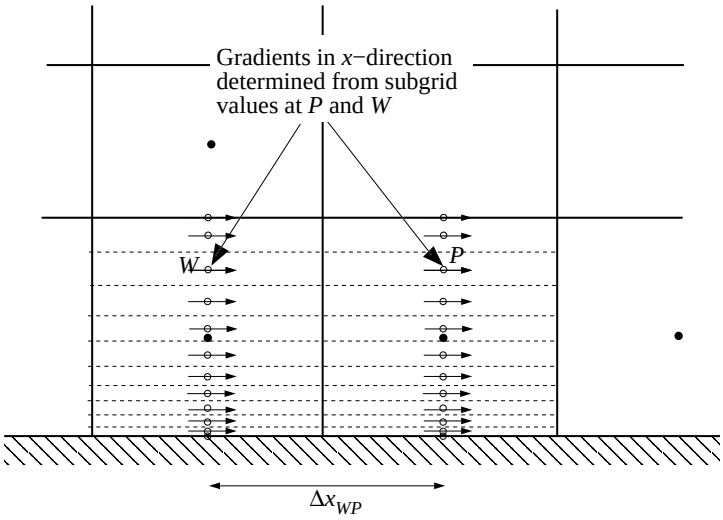

Figure 4.4: Calculation of subgrid convection parallel to the wall

The convection term is added into the source term of the discretized transport equations by first integrating the convection term over the subgrid control volume and introducing a minus sign, since convection appears on the left-hand-side of the transport equation (Equation 4.46):

$$S = -\rho U_P \frac{(\phi_P - \phi_W)}{\Delta x_{PW}} \Delta Vol \qquad \text{for} \quad U_P > 0 \tag{4.63}$$

[3]Since the distance between the upstream node W and current node P is employed, Δx_{PW}, it is the *gradient* that is upwinded rather than just the nodal values. Effectively, one is calculating the gradient in Equation (4.62) using central differencing at the upwind western cell face. In tests with the impinging jet flow, this gave practically identical results to those obtained by upwinding only the values of ϕ, i.e. using:

$$\rho U \frac{\partial \phi}{\partial x} = \rho U_P \frac{(\phi_P - \phi_W)}{\Delta x_{ew}}$$

[4]The storage requirements should be somewhat less than a low-*Re* calculation as pressure is not stored in the subgrid and the number of nodes employed by the wall function approach is likely to be slightly lower.

$$S = -\rho U_P \frac{(\phi_E - \phi_P)}{\Delta x_{EP}} \Delta Vol \qquad \text{for} \quad U_P < 0 \tag{4.64}$$

Rearranging these expression in terms of coefficients of ϕ_P, ϕ_E and ϕ_W:

$$S = -\rho U_P \frac{\phi_P}{\Delta x_{PW}} \Delta Vol + \rho U_P \frac{\phi_W}{\Delta x_{PW}} \Delta Vol \qquad \text{for} \quad U_P > 0 \tag{4.65}$$

$$S = -\rho U_P \frac{\phi_E}{\Delta x_{EP}} \Delta Vol + \rho U_P \frac{\phi_P}{\Delta x_{EP}} \Delta Vol \qquad \text{for} \quad U_P < 0 \tag{4.66}$$

The source S can then be split into s_U and s_P terms as follows:

$$S = s_U + s_P \phi_P \tag{4.67}$$

where the coefficient associated with ϕ_P is included in s_P:

$$\left.\begin{aligned} s_U &= \frac{\rho U_P \phi_W}{\Delta x_{PW}} \Delta Vol \\ s_P &= -\frac{\rho U_P}{\Delta x_{PW}} \Delta Vol \end{aligned}\right\} \quad \text{for} \quad U_P > 0 \tag{4.68}$$

$$\left.\begin{aligned} s_U &= -\frac{\rho U_P \phi_E}{\Delta x_{EP}} \Delta Vol \\ s_P &= \frac{\rho U_P}{\Delta x_{EP}} \Delta Vol \end{aligned}\right\} \quad \text{for} \quad U_P < 0 \tag{4.69}$$

The s_P terms are always negative, and so they always increase the coefficient of ϕ_P and hence the magnitude of the leading diagonal term in the matrix of coefficients, maximizing stability.

Convection perpendicular to the wall in non-conservative form is written:

$$\rho V \frac{\partial \phi}{\partial y} \tag{4.70}$$

A number of different approaches to obtaining the subgrid wall-normal V-velocity profile were explored during the development of the wall function. The most general of these methods relies upon continuity which for a Cartesian arrangement is written:

$$\frac{\partial U}{\partial x} + \frac{\partial V}{\partial y} = 0 \tag{4.71}$$

The process of calculating the wall-normal velocity, V, at each of the nodes across the subgrid is described schematically in Figure 4.5. The process begins in the subgrid cell immediately adjacent to the wall. It is known that the wall-normal velocity at the wall surface is zero, for a non-porous wall, so the mass flux through the south, east and west faces are known. One can then calculate the wall-normal velocity at the northern boundary of the wall-bounded subgrid cell from continuity. This

calculation can be repeated for each subgrid cell from the wall to the outer subgrid boundary.

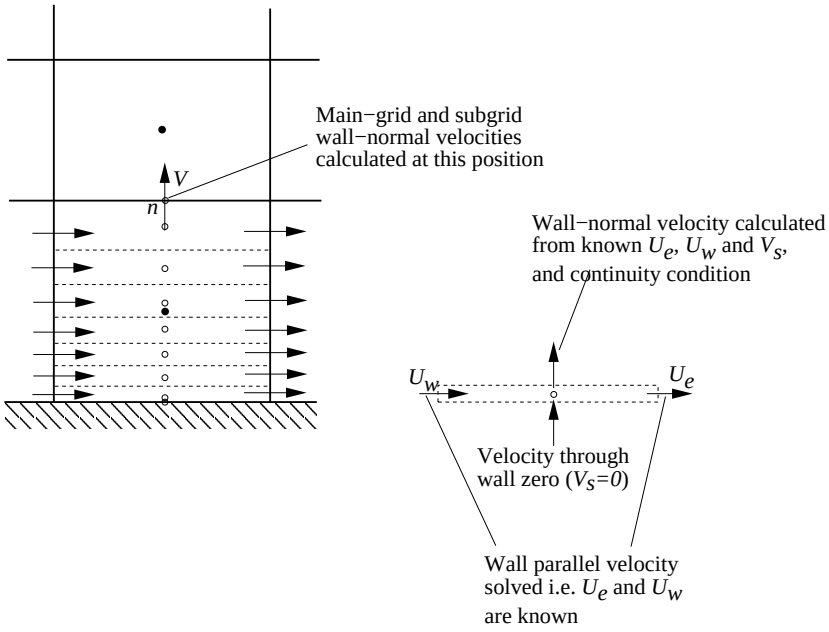

Figure 4.5: Subgrid and main-grid arrangement showing method for calculating the wall-normal velocity from continuity condition in the subgrid cell bounded by the wall

Both subgrid and main-grid wall-normal velocities are calculated at the outer subgrid boundary: the former using the procedure outlined above; the latter from a straightforward interpolation between the nodal values[5]. However, since the integrated subgrid mass fluxes across the east and west faces may not be equal to the corresponding main-grid fluxes parallel to the wall, the subgrid and main-grid wall-normal velocities may not be equal at the outer subgrid boundary (position *n* shown in Figure 4.5). In tests with the impinging jet flow there was, indeed, a mis-match between the main-grid wall-normal velocity at the position *n* and the subgrid value calculated as above (see Figure 4.6). Clearly it is undesirable to have inconsistency between main-grid and subgrid boundary conditions. The subgrid V-velocity profile is therefore scaled with the ratio of the main-grid to the subgrid V-velocity:

$$V_P = \alpha V_P^* \tag{4.72}$$

where the constant, α is given by:

$$\alpha = \frac{V_n'}{(V_n^* \pm tiny)} \quad -3 < \alpha < 3 \tag{4.73}$$

where P denotes the subgrid nodal value, $*$ denotes the subgrid velocities calculated from continuity within the subgrid and the prime ($'$) denotes main-grid value. The constant, α, is evaluated at the outer

[5]The main-grid velocity only needs to be interpolated from main-grid nodal values when a collocated storage arrangement is used. In a staggered grid arrangement, interpolation is unnecessary as the wall-normal V-velocity is calculated at the cell face (position *n*).

subgrid boundary (position n in Figure 4.5). The arbitrary small number *tiny*, which is of the same sign as V_n^*, is included to prevent a singularity occurring as V_n^* approaches zero. In a simple channel flow where the wall-normal velocity is practically zero, the scaling factor can fluctuate between comparatively large positive and negative values as the calculation converges (e.g. $\alpha = \pm 500$) which destabilizes the subgrid solution. To improve the stability the scaling factor α is therefore limited to ± 3. In the impinging jet flow, where there is a significant wall-normal velocity, the maximum calculated value of α was approximately 1.2, and so one would not expect the limit imposed on α to have any adverse affects in other flows. Near-wall V-velocity profiles calculated using the above approach show good agreement with those of low-Reynolds-number models (see Figure 4.6).

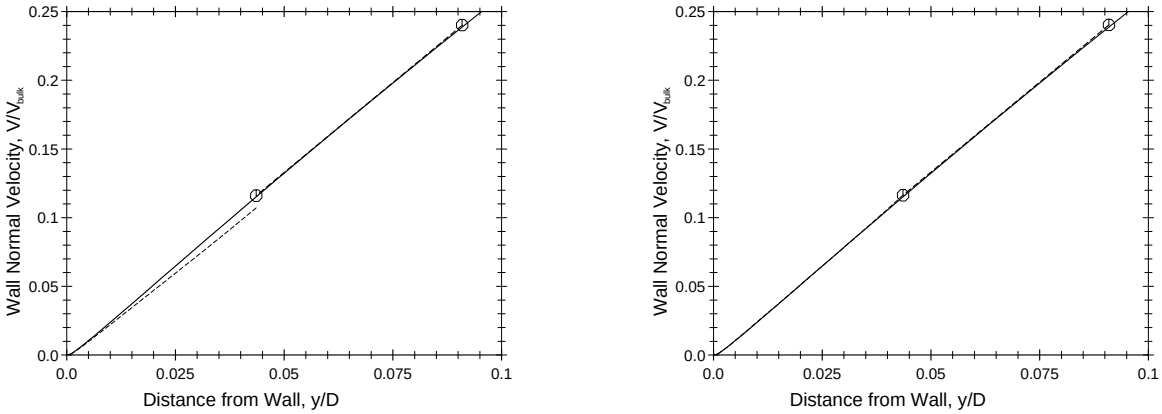

Figure 4.6: Wall normal velocity profiles at the stagnation point of the impinging jet obtained using the linear $k-\varepsilon$ model and standard Yap correction. —-: low-Reynolds-number model; - - -: UMIST-*N* wall function ; $\ominus$: position of main-grid cell faces. The wall-normal subgrid V-velocity is calculated from continuity without scaling on the left-hand plot and with scaling on the right-hand plot (using Equation 4.72). The subgrid profile is shown between the wall (at $y/D = 0$) and the main-grid cell face (at $y/D \approx 0.045$). On the right-hand plot the broken line of the subgrid wall-normal velocity is obscured by the solid line of the low-*Re* model.

Once the V-velocity profile is known, the convection normal to the wall can be calculated. Using an upwind scheme and assuming the V-velocity to be positive (from south to north), convection normal to the wall is discretized as:

$$\rho V \frac{\partial \phi}{\partial y} = \rho V_P \frac{(\phi_P - \phi_S)}{\Delta y_{PS}} \tag{4.74}$$

where ϕ_P and ϕ_S are the subgrid values of U, k, $\tilde{\varepsilon}$ or T evaluated at the current and south subgrid nodes (see Figure 4.3). Integrating convection over the control volume and introducing a negative sign, since the convection term is moved from the left- to the right-hand-side of the Equation (4.46), leads to the following expressions:

$$S = -\rho V_P \frac{(\phi_P - \phi_S)}{\Delta y_{PS}} \Delta Vol \qquad \text{for} \quad V_P > 0 \tag{4.75}$$

$$S = -\rho V_P \frac{(\phi_N - \phi_P)}{\Delta y_{NP}} \Delta Vol \qquad \text{for} \quad V_P < 0 \tag{4.76}$$

The source S can now be split into s_P and a contribution which is introduced into the coefficients a_N and a_S, as follows:

$$\left.\begin{aligned} s_P &= -\frac{\rho V_P}{\Delta y_{PS}}\Delta Vol \\ a_N &= 0 \\ a_S &= \frac{\rho V_P}{\Delta y_{PS}}\Delta Vol \end{aligned}\right\} \quad \text{for} \quad V_P > 0 \tag{4.77}$$

$$\left.\begin{aligned} s_P &= \frac{\rho V_P}{\Delta y_{NP}}\Delta Vol \\ a_N &= -\frac{\rho V_P}{\Delta y_{NP}}\Delta Vol \\ a_S &= 0 \end{aligned}\right\} \quad \text{for} \quad V_P < 0 \tag{4.78}$$

The source term s_P is always negative and hence when s_P is taken over to the left-hand-side of the discretized equation the coefficient a_P (i.e. the leading diagonal elements in the matrix of coefficients) is increased, enhancing stability.

4.3.2 Under-Relaxation

In all of the test-cases considered in this thesis it has been found that no under-relaxation of the wall-parallel momentum or temperature equations is necessary (i.e. $\alpha_U = \alpha_T = 1.0$). A modest amount of under-relaxation of the subgrid k and $\tilde{\varepsilon}$ equations is necessary, typically $\alpha_k = \alpha_\varepsilon = 0.85$. No under-relaxation is required in the subgrid temperature equation since none of the source terms (s_U) appearing in the TDMA are dependent upon the values of ϕ_P. For the momentum equations, there is obviously some feedback through the strain-dependent P_k modifying the eddy-viscosity, and in curvilinear coordinates there are additional geometric source terms which are added into s_U, but these effects do not appear to cause stability problems.

In each iteration of the UMIST-*N* wall function, the subgrid boundary conditions are first updated, the coefficient matrix is assembled and then the matrix is solved with one sweep of the TDMA. Because of the under-relaxation, there may be a small discontinuity in the k and $\tilde{\varepsilon}$ profiles at the northern boundary during the early stages of a calculation, caused by the solution lagging behind the updated boundary conditions. This discontinuity is responsible for the stability problems encountered when using the differential length-scale correction at the start of a new calculation, when k and $\tilde{\varepsilon}$ boundary conditions are changing rapidly (as discussed in Section 4.2).

4.3.3 Boundary Conditions

For each variable, two boundary conditions are required for the one-dimensional subgrid equations. On one side, the subgrid domain is bounded by a wall (node $i = 1$), and on the opposite side it joins the main-grid domain (node $i = n$). The subgrid transport equations are solved from nodes $i = 2$ to $(n-1)$ inclusive. In addition, at the ends of a wall, for example on the axis of symmetry in the impinging jet flow, boundary values need to be supplied in the wall-parallel direction to allow the convection terms to be evaluated.

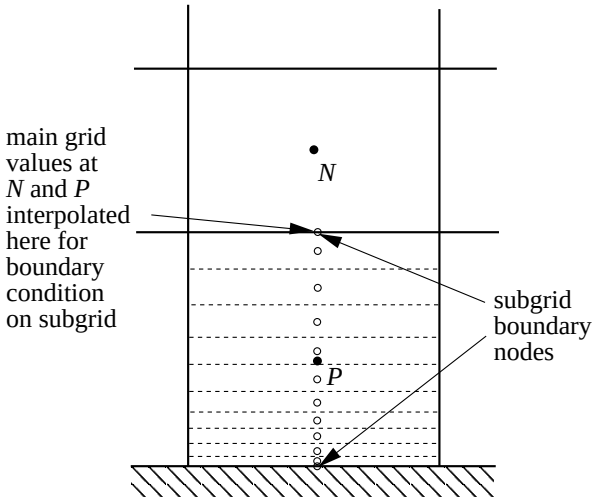

Figure 4.7: Subgrid boundary conditions

Wall Boundary $(i = 1)$

The boundary conditions for the subgrid nodes on the wall are identical to those applied in a low-Reynolds-number solution. U, k and $\tilde{\varepsilon}$ all become zero at the wall (i.e. $U_1 = k_1 = \tilde{\varepsilon}_1 = 0$). There are two common thermal wall boundary conditions: prescribed wall temperature or prescribed wall heat flux. The boundary condition in the former case is trivial since the temperature at the subgrid boundary node is simply set to a prescribed value ($T_1 = T_{wall}$). The wall heat flux can then be calculated from Fourier's law, since the near-wall subgrid cell is within the viscous sublayer. For a wall with constant heat flux, the calculated flux to the boundary is removed (by setting $a_S = 0$ for a wall on the south of the cell) and the given flux is added in as a source term. The wall temperature can then be calculated from Fourier's law.

Free Boundary $(i = n)$

The values of U, k, $\tilde{\varepsilon}$ and T prescribed at the outer (free) boundary, where the subgrid meets the main grid, are interpolated between the two near-wall main-grid nodal values, at P and N, as shown in

Figure 4.7. Although this interpolation may not be desirable in terms of accuracy – assuming a linear variation from node P to node N – the alternative of extending the subgrid only to the main-grid nodal position P (and hence using the calculated values at node P as boundary conditions for the subgrid calculation) introduces significant problems with the calculation of cell-averaged quantities (e.g. $\overline{P_k}$, $\overline{\tilde{\varepsilon}}$). The linear interpolation for the boundary condition does cause a small discrepancy between the main grid and subgrid velocities at P in the log-law plot for a channel flow (see Figure 4.14). Various other interpolation functions were tested but none provided a significant improvement in results whilst maintaining generality. Since k and $\tilde{\varepsilon}$ values are also linearly interpolated, the eddy viscosity $\left(\mu_t = c_\mu f_\mu k^2/\tilde{\varepsilon}\right)$ will not be a linear interpolation of the two near-wall main-grid nodal values. Again, a number of different formulations have been tested, for example, by interpolating the viscosity and obtaining k or $\tilde{\varepsilon}$ from this boundary condition for μ_t, but none of these has been found to provide any improvement upon the simpler practice of interpolating the boundary condition for k and $\tilde{\varepsilon}$ and then calculating μ_t. Assuming a linear variation of U, k, $\tilde{\varepsilon}$ and T between nodes P and N is, moreover, consistent with the assumptions used in the main-grid.

Wall Ends

A typical example of a wall-end boundary is shown in Figure 4.8. In this case, since the boundary coincides with the edge of the domain, additional subgrid nodes are placed on the boundary itself. Subgrid transport equations are not solved for these boundary nodes: their only purpose is to provide boundary values for computing the convection parallel to the wall and for the calculation of the subgrid wall-normal velocity (for which the mass flux through the boundary face needs to be known). Subgrid end-of-wall boundary values are set in exactly the same manner as in the main-grid calculation. For the axisymmetric case shown in Figure 4.8 this would involve zero-gradient conditions for the wall-normal velocity, k, $\tilde{\varepsilon}$ and T and zero wall-parallel (radial) velocity for the nodes on the axis of symmetry.

4.3.4 Subgrid Residuals

The subgrid nodal residual is calculated as follows:

$$R_\phi = a_P\phi_P - (a_N\phi_N + a_S\phi_S + s_U) \tag{4.79}$$

where ϕ is the relevant variable (U, k, $\tilde{\varepsilon}$ or T). The total subgrid residual for each block is calculated by summing $\left|R_\phi\right|$ over each subgrid domain. One could non-dimensionalize the subgrid residuals and place an upper limit on their value so that the calculation would not be considered converged unless residuals fell below that value. In practice, however, if subgrid residuals are not falling, the residuals in the main-grid will be increasing. Monitoring subgrid residuals is useful, however, in a multiblock calculation when one can identify which wall is causing convergence problems. Additionally, subgrid residuals can be useful if, for instance, one wants to freeze the main-grid solution but continue to run

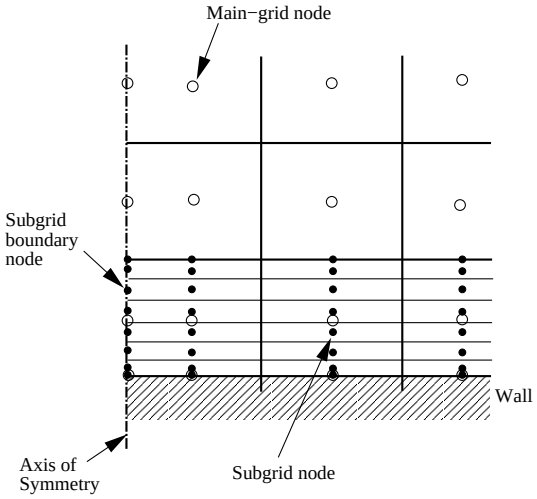

Figure 4.8: Arrangement of subgrid nodes at the end of a wall.

the subgrid calculation to ensure that it converges.

4.3.5 Calculation of Wall-Function Parameters

In standard wall-function treatments, such as that proposed by Chieng & Launder [49], the wall function provides values for:

- wall shear stress, τ_{wall}
- average kinetic energy production, $\overline{P_k}$
- average dissipation rate, $\overline{\varepsilon}$
- nodal dissipation rate, ε_P
- wall temperature, T_{wall}, or wall heat flux, q_{wall}

In such treatments, the momentum equation is solved in the near-wall cell with τ_{wall} included as a source term (having suppressed the internally calculated flux to the wall by setting $a_S = 0$ for a southern wall). The kinetic energy equation is solved in the near-wall cell with production and dissipation terms replaced by $\overline{P_k}$ and $\overline{\varepsilon}$ respectively, and the diffusive flux is set to zero ($a_S = 0$ as before). The dissipation rate equation is not solved in the near-wall cell, but instead the value ε_P is prescribed at the near-wall node.

In the UMIST-*N* wall function, momentum, kinetic energy *and* isotropic dissipation rate equations are solved in the near-wall cells. There is thus no need to prescribe ε_P. Such an approach might lead to instabilities in any case, since the $\tilde{\varepsilon}$-equation solved in the subgrid would be strongly linked to ε_P through the boundary conditions. The new wall function therefore needs to provide values of the following parameters:

- wall shear stress, τ_{wall}
- average kinetic energy production, $\overline{P_k}$
- average total dissipation rate, $\overline{\varepsilon}$
- average production rate of $\tilde{\varepsilon}$, $\overline{(P_k\tilde{\varepsilon}/k)}$
- average dissipation rate of $\tilde{\varepsilon}$, $\overline{(f_2\tilde{\varepsilon}^2/k)}$
- average gradient production $\overline{P_{\varepsilon 3}}$
- average near-wall length scale correction (Yap correction), $\overline{Y_c}$
- wall temperature, T_{wall}, or wall heat flux, q_{wall}

The wall shear stress, τ_{wall}, is calculated by assuming a linear velocity profile between the subgrid node adjacent to the wall and the wall itself (i.e. assuming that the near-wall subgrid cell is well within the viscous sublayer). For a stationary wall in 2-*D* Cartesian coordinates this is simply:

$$\tau_{wall} = \mu\frac{U_P}{y_P} \tag{4.80}$$

where subscript P denotes the value at the subgrid node adjacent to the wall and μ is the molecular viscosity. In a similar manner, the heat flux, q_{wall}, can be calculated from Fourier's heat conduction law:

$$q_{wall} = -\lambda\frac{\partial T}{\partial y} = -\frac{\mu c_p}{\sigma}\frac{\partial T}{\partial y} \tag{4.81}$$

which can be rearranged to give:

$$T_{wall} = T_P + \frac{\sigma q_{wall} y_P}{\mu c_p} \tag{4.82}$$

or:

$$q_{wall} = \frac{\mu c_p (T_{wall} - T_P)}{\sigma y_P} \tag{4.83}$$

As with standard wall functions, the subgrid values of τ_{wall} and q_{wall} replace the diffusive fluxes in the main-grid and so one should set $a_S = 0$ in the momentum and temperature equations.

Average source terms for k and $\tilde{\varepsilon}$ are evaluated by assuming the subgrid values to be constant over the extent of each subgrid cell and equal to the subgrid nodal value. If the subgrid node on the wall surface is $i = 1$ and that on the outer subgrid boundary node $i = n$, then the average production term for a simple 2-*D* Cartesian grid is given by:

$$\overline{P_k} = \frac{\sum_{i=2}^{n-1}(P_k\Delta y)_i}{\sum_{i=2}^{n-1}(\Delta y)_i} \tag{4.84}$$

where $(P_k\Delta y)_i$ is the product of the production rate and the cell thickness for subgrid cell i, and $\sum_{i=2}^{n-1}(\Delta y)_i$ is the total thickness of the subgrid (which is equal to the thickness of the main-grid cell).

The main-grid momentum and heat fluxes to the wall are replaced by values calculated from the subgrid solution (τ_{wall} and q_{wall}). To be entirely consistent with this treatment one should also replace the diffusive fluxes of k and $\tilde{\varepsilon}$ to the wall in the main-grid calculation with values obtained from the subgrid solution. Tests in channel and impinging flows showed that these fluxes are negligible in comparison to other terms in the main-grid k and $\tilde{\varepsilon}$ equations and hence one can just set $a_S = 0$ (for a southern wall) in the main-grid near-wall cell for the k and $\tilde{\varepsilon}$ equations.

When the NLEVM is used, one needs to evaluate strain-rates and vorticity at grid nodes in order to calculate nodal values of the c_μ function and the non-linear stress components, described in Section 2.3. Throughout the main-grid flow domain the nodal strain-rates and vorticity are calculated based on values of velocity at the cell boundaries, assuming a linear velocity profile across the cell. Whilst this practice may be sufficiently accurate across most of the flow domain, the assumption of a linear velocity profile across the near-wall main-grid cell is inappropriate if one is using wall functions. For the near-wall main-grid cell, the subgrid velocity distribution gives a more accurate picture of the strain-rate and vorticity at the main-grid node P. Therefore, the subgrid strain-rates and vorticity are evaluated and interpolated to the main-grid node position. These subgrid values are then used to find the value of c_μ and the non-linear stress components at the main-grid node P.

4.3.6 Generating the Subgrid Mesh

The subgrid transport equations described in Section 4.2 are solved over an algebraically generated grid within the main-grid near-wall cell. In order to obtain sufficient resolution of the peaks of k and $\tilde{\varepsilon}$ it is necessary to cluster subgrid nodes towards the wall. A schematic diagram of a simple 2-D Cartesian subgrid is given in Figure 4.9. The distance from the wall to the face of subgrid cell i is given by y_i and to the subgrid node y_i^p. The locations of the bottom and top of the subgrid (locations y_1 and y_7, respectively) are known from the main-grid coordinates. Between nodes $i = 1$ and $i = 7$ (from the wall to the top edge of the domain), the subgrid is expanded with a given ratio, r, according to:

$$\Delta y_i = r\Delta y_{i-1} \tag{4.85}$$

where Δy_i is the cell width for node i. The distance between the first and last boundary locations consists of the sum of the control volume widths:

$$\begin{aligned} y_n - y_1 &= \Delta y + r\Delta y + r^2\Delta y + \ldots + r^{(n-3)}\Delta y \\ &= \sum_{m=0}^{n-3} r^m \Delta y \end{aligned} \tag{4.86}$$

where n is the number of nodes, in this case $n = 7$. The width of the smallest control volume $(\Delta y = y_2 - y_1)$ is then given by:

$$\Delta y = \frac{y_n - y_1}{\sum_{m=0}^{n-3} r^m} \tag{4.87}$$

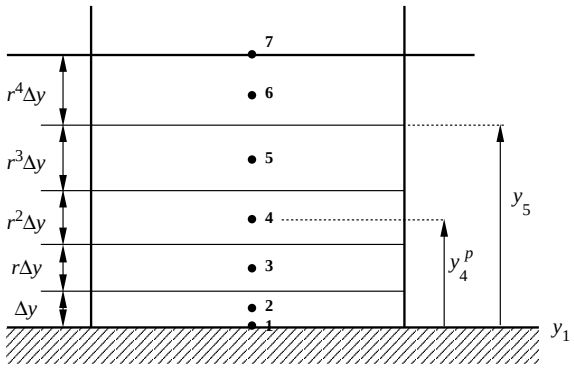

Figure 4.9: Two-dimensional Cartesian subgrid mesh showing node numbers and cell widths.

One can then calculate the position of the cell faces in recursive fashion:

$$y_m = y_{m-1} + r^{(m-2)}\Delta y \quad \text{for} \, m = 2,3,4...(n-2) \tag{4.88}$$

Finally, the subgrid nodes are positioned in the centre of the cells, i.e.:

$$y_m^p = \frac{(y_m + y_{m-1})}{2} \quad \text{for} \, m = 2,3,4...(n-1) \tag{4.89}$$

Following common practice, it should be ensured that the solution is independent of the subgrid mesh. The expansion ratios and number of subgrid nodes should be adjusted until there is no significant difference in computed results. In tests with the impinging jet flow where the main-grid near-wall node y^+ values varied from 230 at the stagnation point to 35 at 6 diameters downstream, a minimum of 30 subgrid cells with an expansion ratio of 1.15 was required to achieve a subgrid-independent solution. However, relatively large expansion ratios were found to introduce stability problems with the NLEVM and, in practice, a maximum ratio of 1.10 was used with a corresponding slight increase in the number of subgrid nodes to maintain the same near-wall y^+values.

4.3.7 Multiblock Implementation

In order to generate structured grids around complex shapes it is sometimes necessary to decompose the grid into a number of blocks. This approach was used in the STREAM code to study the flow around the Ahmed car body (see Figure 7.10). Since the UMIST-*N* wall function uses wall-parallel gradients for convection and for the calculation of the wall-normal velocity from continuity, it is necessary to use a multiblock implementation of the wall function if walls extend over more than one block. In order to implement the multiblock wall function in an efficient manner, it is useful to consider the issues of block addressing, halo nodes and block-to-block swapping of boundary conditions at an early stage in the design of the wall-function code.

Communication of data (i.e. nodal values of U, V, W, k, $\tilde{\varepsilon}$ and T) between blocks is accomplished using halo cells. These are additional nodes tagged on at the end of a block which have physical

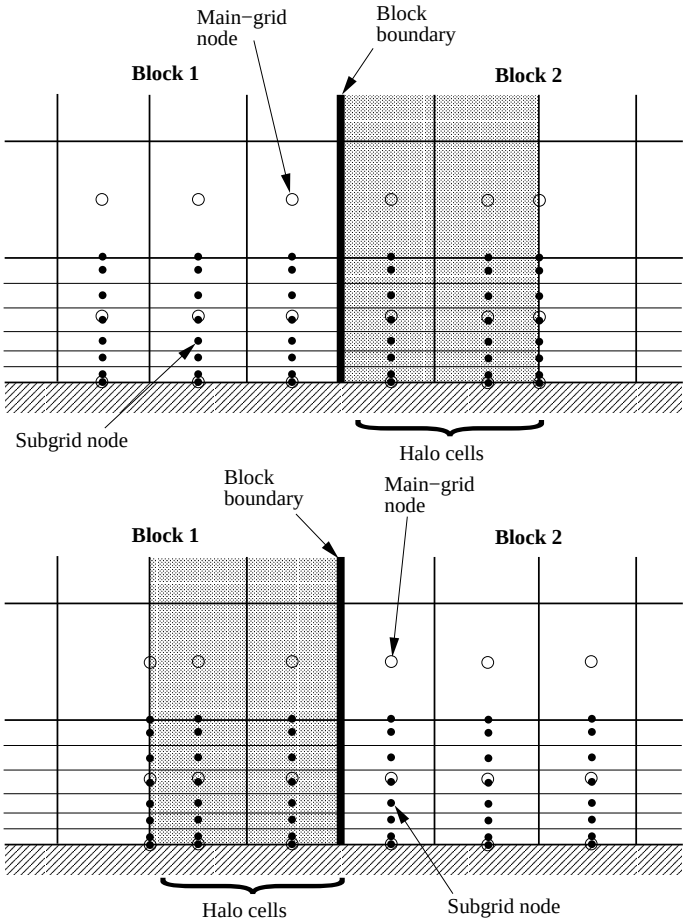

Figure 4.10: Arrangement of subgrid and main-grid nodes at a block interface. The top diagram shows the nodes associated with Block 1, including the halo nodes. The lower diagram shows the nodes associated with Block 2.

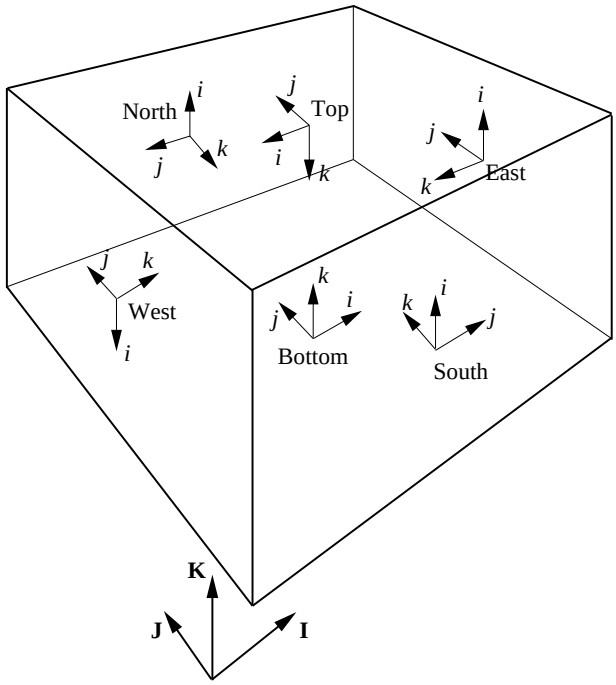

Figure 4.11: Three-dimensional block arrangement showing face labels, main-grid coordinates (in upper-case bold) and subgrid coordinates for each face (lower-case italic).

locations identical to nodes in the neighbouring block (see Figure 4.10). Transport equations are not solved for halo node values. Instead, at the beginning (or end) of each iteration, the values of U, V, W, k, $\tilde{\varepsilon}$ and T at the halo nodes are updated from the neighbouring block's values. Halo nodes therefore provide boundary conditions for the cells internal to a block, for which transport equations are solved. The STREAM code uses a total of three layers of halo nodes, as shown in Figure 4.10. Two layers of nodes are required for the calculation of convection using quadratic differencing. The final layer on the cell boundary is only used to define the edge of the domain. The STREAM code version of the UMIST-*N* wall function was designed with exactly the same halo arrangement as the main-grid code (i.e. three layers of cells). This was not strictly necessary, since the UMIST-*N* wall function only employs upwind differencing, but it was conceptually simpler to keep the same domain size.

Wall functions may be employed on many faces within each block (north, south, east etc.). Rather than code six different versions of the UMIST-*N* wall function, one for each face, a single solution procedure is coded with a local subgrid coordinate frame. This local coordinate frame is specified so that the subgrid ζ-direction is always in the non-wall-parallel direction and increases with distance from the wall (in most cases this means simply that the subgrid ζ-axis is wall-normal and points into the domain from the wall surface). Figure 4.11 shows a single main-grid block with coordinate frame denoted in upper-case bold (**I**, **J**, **K**). Associated with each of the faces of the block are also shown subgrid coordinate frames, denoted in lower-case italic (i, j, k).

To specify fully how two main-grid blocks are joined together, one needs to identify the faces

through which the two blocks are mated and also how the coordinate frames transform between blocks. For instance, the entire south face on Block (1) could be attached to the entire east face on the neighbouring Block (2), with the coordinate frame in Block (1), **(I**, **J**, **K)**, being equivalent to the coordinate frame **(–K**, **I**, **–J)** in Block (2). This specification will be well known to those already using multiblock domain decomposition. In addition to these details, however, one has to be careful when walls continue over two or more neighbouring blocks that the coordinate frames used in the subgrid wall function domains are correctly matched together (bearing in mind that there is a different subgrid coordinate frame according to the face on which the wall is positioned). This is particularly important as the UMIST-*N* wall function uses grid-aligned velocity vectors so that the U-velocity in one block may be equivalent to the V-velocity in a neighbouring block. It is not difficult to work out the permutations of block faces, main-grid coordinate frames and subgrid coordinate frames, and the particular algorithm used will depend on how the multiblock domain decomposition is already coded for the main-grid. In order to provide some assistance to future researchers, a simple cut-out diagram is provided in Figure 4.12 which can be glued together into a cube. The faces of the cube give the subgrid *i*- and *j*-axes and the *k*-axis always acts into the cube. The main-grid (**I**, **J**, **K**) are also provided along with the names of the block faces. In the authors' experience, such cubes are invaluable for examining how to specify the correct transformation between two subgrid coordinate frames.

Finally, it should be mentioned that when coding the subgrid wall function it is inefficient to store values in multi-dimensional arrays and specify a particular subgrid node directly from its wall number[6] and its (i, j, k) coordinates. This approach may lead to excessive storage requirements for the subgrid arrays when, for instance, the *i*-axis on one wall contains twice as many nodes as the *i*-axis on another wall. Instead, an efficient subroutine or function can be written which converts wall number and (i, j, k) coordinates into a single subgrid node number, say (ns), which then increments sequentially from 1 to *nsmax*, where *nsmax* is the total number of subgrid nodes. The subgrid data is then stored as one-dimensional arrays with dimension *nsmax*, rather than as multi-dimensional arrays of size $(imax \times jmax \times kmax)$ times the number of walls.

4.3.8 Solution Sequence

The first step in the subgrid wall function is to define the subgrid mesh and any geometric parameters that are used by the subgrid wall function (a particular consideration if one is using non-orthogonal curvilinear coordinates). This is performed only once, at the beginning of a calculation, just after the main-grid mesh has been defined. In each subsequent main-grid iteration, before the main-grid coefficient matrices are assembled, the following sequence of events is followed:

1. Initialize the one-dimensional subgrid variable arrays from a previous subgrid iteration, previous subgrid solution (used as a starting point) or initial profile.

[6] where each wall face in each block is assigned sequentially a separate wall number.

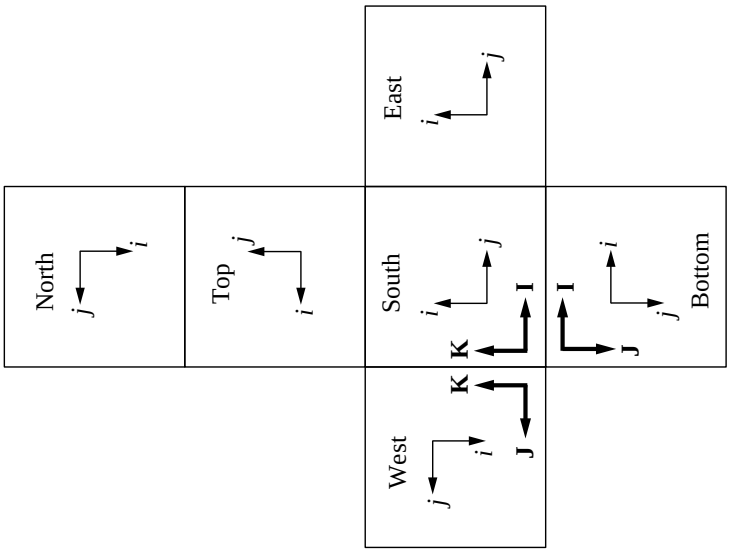

Figure 4.12: Unfolded representation of three-dimensional block arrangement showing face labels, main-grid coordinates (in upper-case bold) and subgrid coordinates for each face (lower-case italic). Once the diagram is cut-out and glued together into a cube with the writing on the outside of the box, the subgrid *k*-axis always acts in the direction into the box

2. Calculate the subgrid eddy-viscosity, μ_t, and source terms for the wall-parallel momentum, k, $\tilde{\varepsilon}$ and temperature equations.

3. Assemble the subgrid coefficient matrices for each of the transport equations and solve each in turn with one sweep of the TDMA.

4. Calculate wall-function parameters to be passed to the main-grid flow solver (τ_{wall}, average source and sink terms in the k and $\tilde{\varepsilon}$ equations, and T_{wall} or q_{wall}).

5. Repeat steps 1 – 4 for each of the main-grid cells along the length of the wall.

It is important, especially when using the strain-dependent c_μ function with the Craft *et al.* NLEVM that boundary conditions are only updated after c_μ and the non-linear stresses have been calculated. Otherwise, the updated velocity boundary value can lead to significant strain-rates across the subgrid cell adjacent to the boundary which may cause instability through the feedback mechanism of $(c_\mu \rightarrow \mu_t \rightarrow S \rightarrow c_\mu)$, as mentioned in Chapter 2.

4.4 Validation: Channel Flow Results

One advantage of the UMIST-*N* wall function is that it is relatively straightforward to reconfigure the code to run as a stand-alone 1-*D* parabolic solver, which can then be tested in simple flows to ensure that it has been coded correctly. The wall-function code was adjusted to run a fully-developed channel flow simulation with the subgrid region extending across the whole flow domain. The Reynolds

number, based on bulk velocity and channel width (wall to wall), was $Re = 100,000$. Results were compared to low-Reynolds-number model results obtained from the 2-*D* elliptic solver, TEAM, using the Launder-Sharma $k-\varepsilon$ model. An identical distribution of subgrid nodes was used as for the low-*Re* model with 110 nodes, clustered towards the wall. The wall function and low-*Re* model results were found to be identical (Figure 4.13).

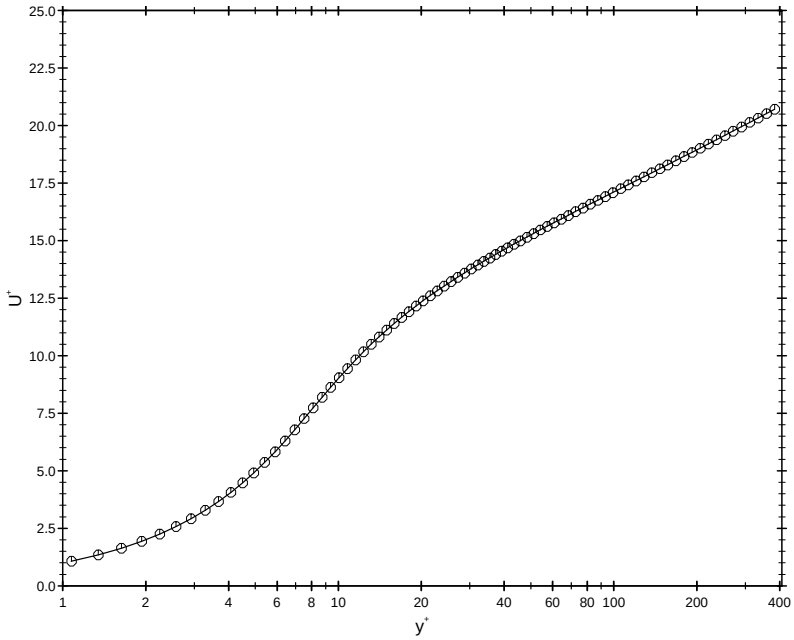

Figure 4.13: Comparison the semi-logarithmic velocity profiles for a fully-developed channel flow at $Re = 100,000$; —-: TEAM 2-*D* elliptic solver; symbols: UMIST-*N* wall function configured as parabolic solver.

Following these tests, the performance of the UMIST-*N* wall function was assessed in a 2-*D* channel flow with periodic inlet and outlet boundaries and a Reynolds number of $Re = 100,000$. Calculations were made using the TEAM code with the linear Launder-Sharma $k-\varepsilon$ model [13]. QUICK differencing was employed for convection of momentum and PLDS for k and $\tilde{\varepsilon}$. A grid with 110 nodes for the half-channel width in the wall-normal direction was used for low-*Re* model simulations and results were tested to ensure that they were fully grid-independent. Two different grid arrangements were used for the wall-function calculations which corresponded to near-wall nodal y^+ values of approximately 30 and 80. Across the subgrid domain, 40 nodes were used with an expansion ratio of 1.1 which was sufficient to obtain a subgrid-independent solution. Figure 4.14 shows the profiles of U^+ versus y^+ obtained using the UMIST-*N* wall function for the two high-*Re* grids against the results obtained from the low-*Re* model and law-of-the-wall profiles.

The UMIST-*N* wall function results for the channel flow, shown in Figure 4.14, are in good agreement with the low-*Re* results for both near-wall cell sizes. A small discrepancy in the near-wall main-grid nodal velocity is due to the linear interpolation between the two near-wall nodes, used to obtain the subgrid boundary condition. Several other methods of interpolating have been tested for

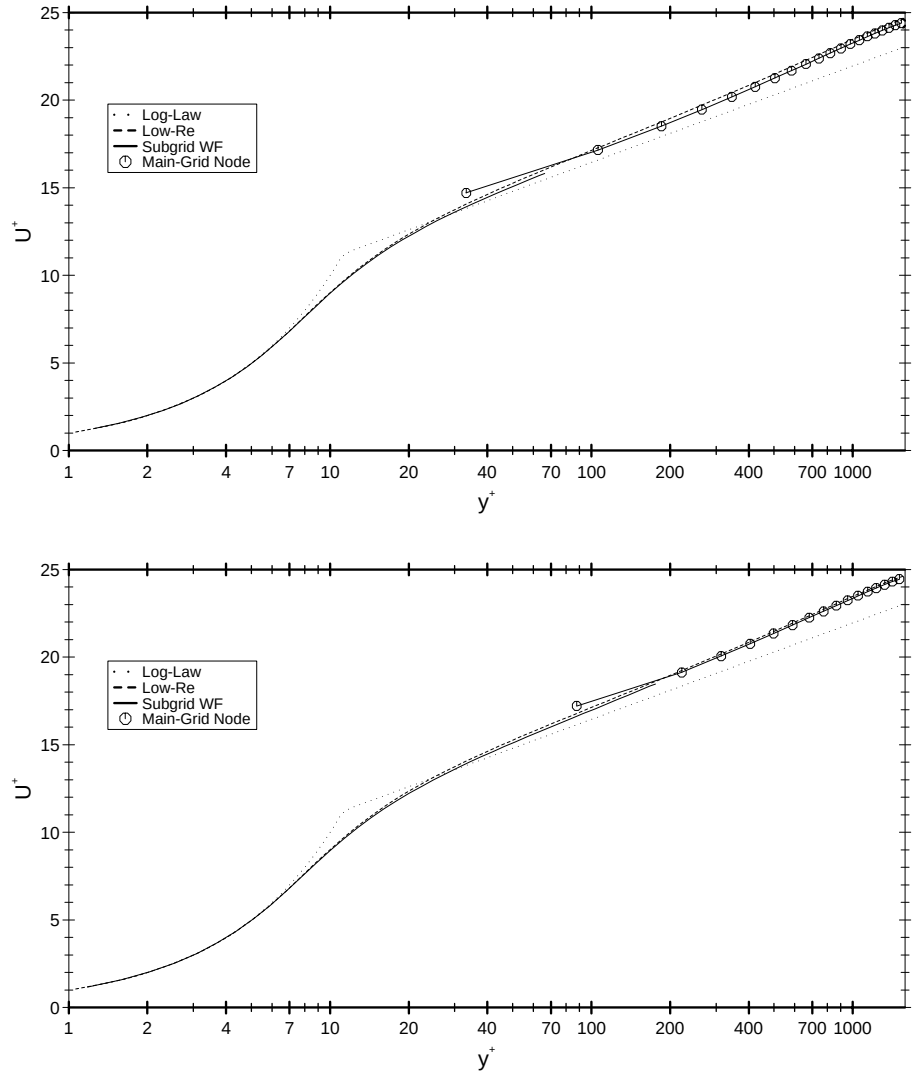

Figure 4.14: UMIST-*N* wall function predictions of the velocity log-law with a near-wall grid arrangement of $y^+ \approx 30$ (top) and $y^+ \approx 80$ (bottom).

the subgrid boundary condition, but none provided any significant improvements without diminishing the generality of the wall function. In any case, within the near-wall cell the subgrid solution provides a more accurate prediction of the velocity profile and this can be used to gain a better picture of the velocity close to the wall if necessary. The results also show little dependence upon the size of the near-wall main-grid cell.

The above tests were carried out using the TEAM code. The UMIST-*N* wall function implementation in the STREAM code was also tested in a fully-developed channel flow before calculations of the Ahmed body were undertaken. The wall function was applied to each of the six possible faces of a block (north, south, east etc.) and results compared to those obtained using a low-*Re* model. Both linear and non-linear $k-\varepsilon$ models were assessed and skewed grids were used to ensure that the calculated subgrid geometric parameters (metric tensors, Jacobians etc.) were correct. The multiblock wall function implementation was also tested by setting up a fully-developed channel flow over two blocks. The relative orientation of the two blocks was then changed to ensure that this had no effect on results.